# The impact of graphene oxide sheet lateral dimensions on their pharmacokinetic and tissue distribution profiles in mice

Dhifaf A. Jasim [a], Leon Newman [a], Artur Filipe Rodrigues [a], Isabella A. Vacchi [b], Matteo A. Lucherelli [b], Neus Lozano [a,c], Cécilia Ménard-Moyon [b], Alberto Bianco [b], Kostas Kostarelos [a,c,*]

[a] Nanomedicine Lab, National Graphene Institute, Faculty of Biology, Medicine & Health, University of Manchester, AV Hill Building, Manchester M13 9PT, United Kingdom
[b] CNRS, Immunology, Immunopathology and Therapeutic Chemistry, UPR3572, University of Strasbourg, Strasbourg 67000, France
[c] Catalan Institute of Nanoscience and Nanotechnology (ICN2), CSIC and BIST, Campus UAB, Bellaterra, 08193 Barcelona, Spain

## ARTICLE INFO

## ABSTRACT

Although the use of graphene and 2-dimensional (2D) materials in biomedicine has been explored for over a decade now, there are still significant knowledge gaps regarding the fate of these materials upon interaction with living systems. Here, the pharmacokinetic profile of graphene oxide (GO) sheets of three different lateral dimensions was studied. The GO materials were functionalized with a PEGylated DOTA (1,4,7,10-tetraazacyclo-dodecane-1,4,7,10-tetraacetic acid), a radiometal chelating agent for radioisotope attachment for single photon emission computed tomography (SPECT/CT) imaging. Our results revealed that GO materials with three distinct size distributions, large (l-GO-DOTA), small (s-GO-DOTA) and ultra-small (us-GO-DOTA), were sequestered by the spleen and liver. Significant accumulation of the large material (l-GO-DOTA) in the lungs was also observed, unlike the other two materials. Interestingly, there was extensive urinary excretion of all three GO nanomaterials indicating that urinary excretion of these structures was not affected by lateral dimensions. Comparing with previous studies, we believe that the thickness of layered nanomaterials is the predominant factor that governs their excretion rather than lateral size. However, the rate of urinary excretion was affected by lateral size, with large GO excreting at slower rates. This study provides better understanding of 2D materials in vivo behaviour with varying structural features.

## 1. Introduction

Graphene and related flat-shaped materials exhibit outstanding properties generated from their unique 2D geometry [1–3]. These materials have attracted great interest from different scientific disciplines [1–3]. The biomedical applicability of graphene has only been researched for the last decade [4]. The available graphene surface area is the largest for any material at the nanoscale, which provides a potential delivery platform for maximum payload of therapeutic molecules and for bio-functionalization with imaging probes [5–8]. The electrical, electronic [9], mechanical, optical properties [8,10,11] and flexibility of graphene based materials [2,12] allow their use as biosensing platforms and offer a great potential for use in regenerative medicine [13] and electroresponsive drug therapy. It also can be useful to meet the

requirements of the electroactive nervous and cardiac systems and therefore provide a means of neuronal and cardiac drug delivery [14]. All these properties offer interesting possibilities of graphene materials following their interaction with soft biological matter [11,15].

Due to the great potential offered by using graphene materials for biomedical applications, it is critical to understand their fate in vivo [16]. Graphene oxide (GO) has expanded the applications of graphene-based materials in biomedicine due to its hydrophilicity and improved compatibility with biological systems. GO has been administered intravenously [17–19], intraperitoneally, orally [20] and intravitreally [21] with no reported toxic effects even after long exposure times [20,21]. After intravenous or intraperitoneal administration, GO has been reported to accumulate in the mononuclear phagocytic system, or as more commonly known the reticuloendothelial system (RES). The

spleen has been reported as the main site for the in vivo degradation of intravenously injected functionalized graphene [22]. GO materials have also been reported to accumulate in the lungs [23,24]. Extensive urinary excretion of GO has been reported in several studies after intravenous (i. v.) injection of functionalized GO sheets in mice [16,20,25–29].

Existing studies have used very different types of GO [30,31] that can result in significantly different biological interactions. These interactions will depend on the type of surface functionalization, functional surface groups and dimensions of the GO sheets [17]. The most popular administration route used in the preclinical development of most nanomaterials for biomedical applications has been the intravenous (i.v.) route, which provides 100% bioavailability and maximum tissue exposure [32]. Many studies have used imaging to study the biodistribution of graphene materials by adding a labelling tag using single photon computed tomography (SPECT/CT) with gamma (γ) emitting isotopes [28,33], positron emission computed tomography (PET/CT) with positron emitting isotopes [27,34] or even fluorescent tags for optical imaging [26,34].

Previously we have demonstrated that the thickness of the graphene material plays a major role in its tissue accumulation and excretion [27], however, no systematic correlation with the GO sheet lateral dimension has been offered. In this study, three highly purified and well characterised graphene oxide materials that differ only in their lateral dimensions were functionalized with a chelating moiety for imaging purposes, namely a DOTA molecule tethered to a polyethylene glycol (PEG) linker. The resulting functionalized materials had three distinct sizes as well (l-GO-DOTA, s-GO-DOTA and us-GO-DOTA). Then, whole-body imaging by SPECT/CT and full pharmacokinetic studies were carried out following i.v. administration of the GO-DOTA materials, coupled with analytical and histopathological analysis of critical organs. This study provided important information on the future design of graphene materials for possible tissue targeting applications.

## 2. Results

### 2.1. Preparation and characterisation of GO and GO-DOTA materials

GO was prepared by a modified Hummers' method under pyrogen-free conditions, as previously described [35–37]. Morphology of GO sheets was characterised by dynamic light scattering (DLS), transmission electron microscopy (TEM) and atomic force microscopy (AFM) (Fig. 1). DLS revealed clear differences in the size distribution curves of the aqueous suspensions of the three types of GO materials (l-GO, s-GO and us-GO). The sonication employed to generate the different lateral size nanosheets (s-GO and us-GO) did not significantly impact their surface charge (Fig. 1A-B).

In order to perform biodistribution studies, the GO materials were functionalized with the chelating agent DOTA, which was attached to a tetra-ethylene glycol [(PEG)$_4$] molecule bearing a free amine group [DOTA(PEG)$_4$-NH$_2$], as described in Scheme 1. The functionalized chelating moiety [DOTA(PEG)$_4$-NH$_2$], is referred to as 'DOTA' for ease throughout the manuscript. Although this process resulted in a decreased nanosheet surface charge (Fig. 1B), DOTA functionalization did not significantly impact the colloidal stability of GO, in agreement with previous observations in physiological media [28]. DLS is not particularly suitable as a technique to determine the dimensions of non-spherical particles [38] and we were not able to obtain reliable DLS data for the DOTA-functionalized material. We emphasised on the structural characterisation of GO sheets before and after DOTA functionalization, performed by TEM and AFM (Fig. 1C-D). The tested materials were composed of sheets with distinct differences in lateral dimensions (i.e. the longest dimension observed of each 2D sheet), which are described in detail in Table S1.

In summary, l-GO is comprised of sheets with lateral dimension between 1 and 35 μm, whilst s-GO sheets range between 30 nm and 1.9 μm. The smallest material (us-GO) was characterised by a narrower size distribution, with lateral dimensions ranging from 10 nm to 550 nm.
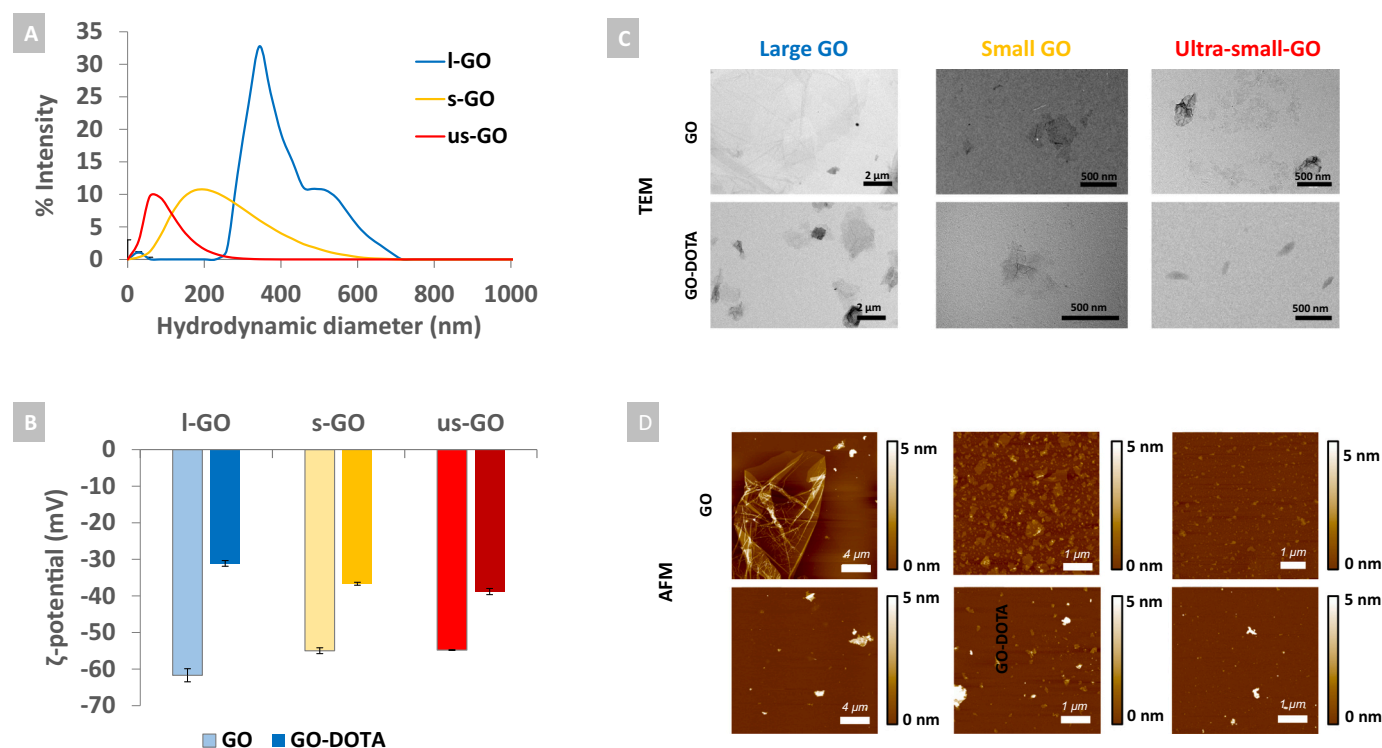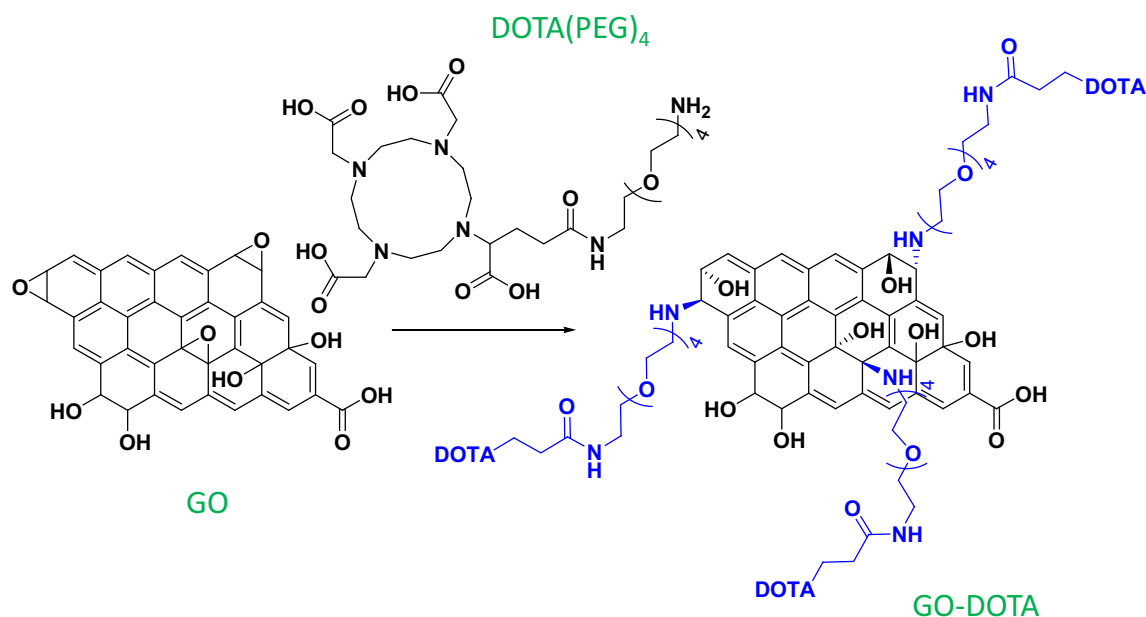


**Fig. 1.** Physicochemical characterisation of l-GO, s-GO and us-GO before and after DOTA functionalisation. A) Dynamic light scattering (DLS) size distributions; B) Electrophoretic mobility (ζ potential) mean surface charge data. Morphological and structural characterisation data is shown, using C) TEM and D) AFM.

**Scheme 1.** Synthesis of GO-DOTA. For the sake of clarity, electrostatic interactions between the protonated amine in $NH_2$-$PEG_4$-DOTA and the carboxylate groups at the edges of GO or in the $PEG_4$-DOTA chain linked to GO are not shown.

Upon functionalisation there was a reduction in the sheet lateral dimension, particularly l-GO-DOTA compared to l-GO, where there was a 5-fold reduction (Table S1). Nevertheless, the lateral dimensions of s-GO-DOTA and us-GO-DOTA sheets remained markedly different from l-GO-DOTA and from each other. These differences could be attributed to the ring opening reaction attacking cooperatively aligned epoxides present in the GO sheet surface, which ultimately create fracture points [39,40]. AFM demonstrated that the thickness of all GO materials had increased following DOTA functionalisation (Table S1). This could be due to the addition of functional groups and has been observed previously in several studies [20,28,41].

The samples were also characterised by X-ray photoelectron spectroscopy (XPS) (Table S1 and Figs. S1–3). The XPS survey table shows ~30–31% oxygen content in all three starting materials. The oxygen content is slightly lower after functionalisation with DOTA, with the introduction of 1.1–1.4% nitrogen content, due to the addition of the DOTA molecule. Similarly, in the oxygen O1s high resolution spectra, there is a clear increase in percentage of the carbonyl peak (Fig. S2). This is due to the introduction of carboxylic acids and amides. On the other hand, the carbon C1s high resolution spectra (Fig. S1) are more complex and revealed changes between the ratio of the carbon region and the carbon-oxygen region. This is often the case after any kind of treatment of GO [42,43] due to the loss of some labile oxygenated functional groups. In particular, the component attributed to C-O-C bonds decreased whereas the C-OH/C-N band increased. These changes suggest that the reaction of epoxide ring opening occurred, thus generating C-OH groups, alongside the introduction of amino groups from the DOTA compound, as previously reported [44]. However, the C-O-C peak did not disappear because of the ether groups in the PEG chain. Two components could be identified in the nitrogen N1s high resolution spectra, namely the amine/amide and the ammonium peaks at ~400 eV and 402 eV, respectively. Both amines and amides are present in the DOTA molecule, further indicating the successful functionalisation of GO with the DOTA moiety (Fig. S3). Thermogravimetric analysis (TGA) also validated chemical functionalisation of GO (Fig. S4). GO starts to lose mass at temperatures even lower than 100 °C due to residual water molecules adsorbed on the GO sheets [37,43,45,46].The two weight losses above 150 °C are due to the oxygenated species present on the surface of GO and to the DOTA molecule in the case of the functionalized materials. The main weight loss occurs at lower temperature (around

220 °C) for the three GO-DOTA compared to the starting materials (~240 °C) was considered another indication of covalent functionalization of the DOTA functionality. The %N obtained by XPS indicated that the three conjugates have a similar DOTA loading. Taken together, these results show that the functionalization of GO with the DOTA derivative was successful and did not cause significant reduction of the starting material.

### 2.2. Efficiency and purity of radiolabeling of [111In]GO-DOTA

The efficiency of radiolabelling of the three types of GO ([111In]l-GO-DOTA, [111In]s-GO-DOTA and [111In]us-GO-DOTA) was compared to control [111In]DOTA in Fig. 2A. The radiolabelling efficiency of the three samples was ~70% at the application point. The samples were purified by removal of unbound [111In]DOTA by centrifugation, reaching a purity of ~90% after centrifugation (Fig. 2B).

### 2.3. Stability of radiolabeling of [111In]GO-DOTA

The three samples had insignificant variable stability in PBS at 37 °C up to 1 week as shown in Fig. 2C, while the samples were stable and retained their radiolabelling purity in 50% serum as shown in the same figure and in Fig. S5. The latter figure demonstrated that the three samples retained a signal at the application point of the TLC compared to the control materials alone [111In]EDTA and [111In]DOTA which moved to the solvent front.

### 2.4. Pharmacokinetics and tissue distribution after i.v. administration

The biodistribution and excretion of the three types of GO ([111In]l-GO-DOTA, [111In]s-GO-DOTA and [111In]us-GO-DOTA) after i.v. administration was studied by SPECT/CT imaging and cut-and-count γ-scintigraphy (Figs. 3, 4 and Figs. S6–9). The levels in blood determined by γ-counting are shown in Fig. 3A. The curve demonstrated that pharmacokinetics for all materials followed two-compartment first order kinetics. The pharmacokinetic parameters are summarised in Table S2 and the values remaining in blood after 1 h are compared to 24 h in Table S3. All three materials were removed from blood very rapidly with only less than 1% of the injected dose remaining in the blood after 24 h. Dynamic SPECT/CT imaging was carried out during the i.v.
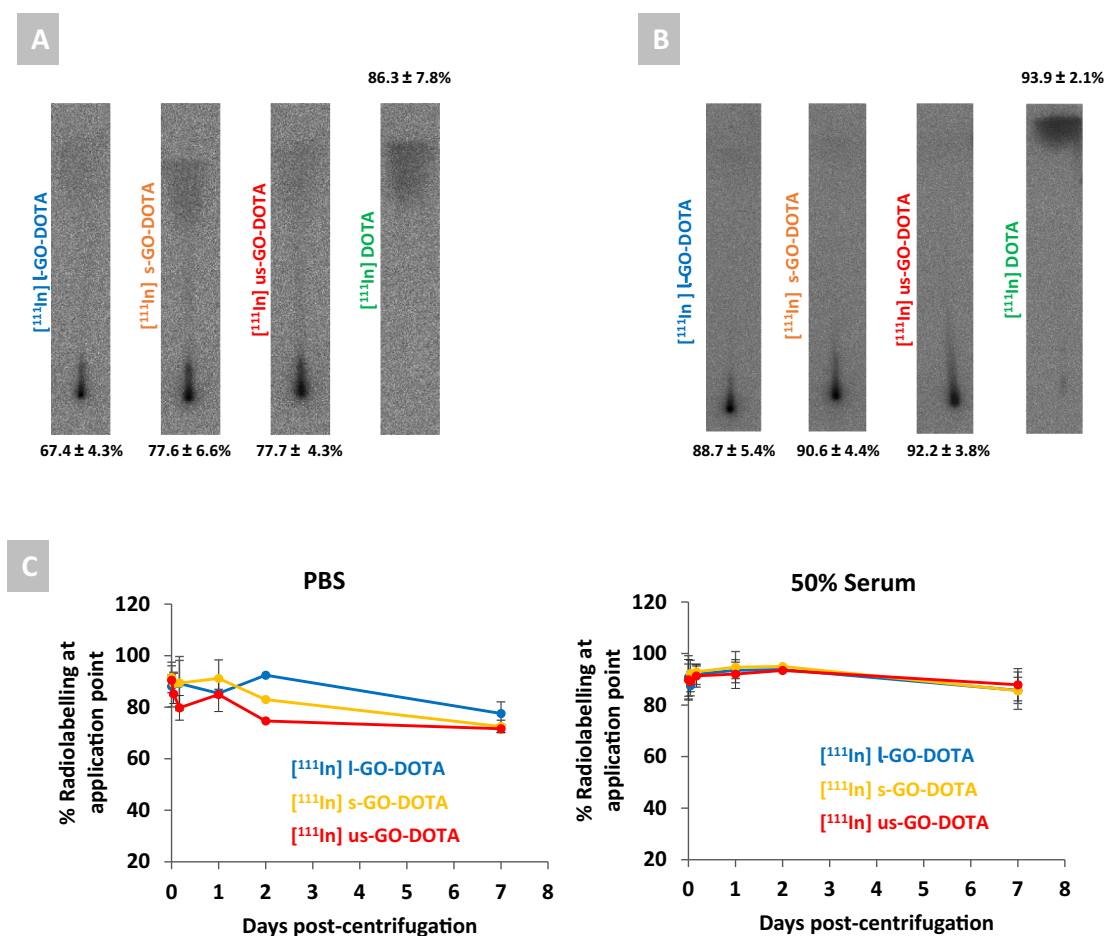
**Fig. 2.** Radiolabelling efficiency and stability. A) Efficiency of radiolabelling of the three types of GO ([$^{111}$In] l-GO-DOTA, [$^{111}$In] s-GO-DOTA and [$^{111}$In] us-GO-DOTA) compared to control [$^{111}$In]DOTA after the radiolabelling reaction; values indicate the average of three independent labelling repeats. B) Radiolabelling purity of the three samples after centrifugation and before administration in the animals. C) Stability of radiolabelling in PBS and 50% serum up to 7 days.

administration of the materials (Fig. S6). The first panel shows the 2 min phase of injection (movie can be played online), showing the delivery from the tail vein and through the vena cava then through whole blood. All three materials ([$^{111}$In]l-GO-DOTA, [$^{111}$In]s-GO-DOTA and [$^{111}$In] us-GO-DOTA) and the control [$^{111}$In]DOTA start to accumulate in the organs within the first hour as demonstrated in the planer images in the second panel in the same figure. Organ accumulation is very evident after 4 h and 24 h (last two panels, Fig. S6). Time activity curves for each material are presented in Fig. S7, indicating a huge accumulation of the larger material ([$^{111}$In]l-GO-DOTA) in the lungs, while the other two materials accumulated mainly in the liver and spleen. All three materials presented bladder and kidney signals at early time points. The control sample [$^{111}$In]DOTA was totally excreted after 1 h with huge bladder signal compared to the other materials (Fig. S7).

These results were further confirmed by a separate experiment using 3D SPECT/CT for better image resolution as demonstrated in Fig. 3B and Fig. S8 for the first batch of mice and Fig. S9 for a second batch of mice. The scale bars are expressed in percentage of injected dose (%ID) per gram of tissue in Fig. 3B and Fig. S9, while it is expressed in MBq in Figs. S8 and S10. These images show minor intestinal signals in all mice. Expression in %ID per gram of tissue will show the minute amounts in blood levels in light organs. The total remaining amounts in the whole body after 24 h quantified from the SPECT images are presented in Table S4, with 50.8%, 36.5% and 38.1% for [$^{111}$In]l-GO-DOTA, [$^{111}$In]s-GO-DOTA and [$^{111}$In]us-GO-DOTA, respectively.

The whole-body SPECT/CT imaging data were validated by a separate cut and count experiment counting the %ID per whole organ of

[$^{111}$In]GO-DOTA or %ID per gram of tissue measured by γ-scintigraphy in a separate experiment with at least 4 mice per condition (Fig. 3C).The data confirmed the same pattern of the SPECT/CT data with lung accumulation for the largest material ([$^{111}$In]l-GO-DOTA) and liver and spleen accumulation for the all three materials ([$^{111}$In]l-GO-DOTA, [$^{111}$In]s-GO-DOTA and [$^{111}$In]us-GO-DOTA). Some kidney and bladder signals were detected at early time points, while minute intestinal signal was evident at the later time points. Very little signals were detected in the control sample (Fig. 3C, bottom row).

### 2.5. Urinary and faecal excretion

Urinary and faecal excretion was studied by collecting the urine and faeces of injected mice to further examine the extent of elimination of the three materials (Fig. 4). Pooled urine samples ($n = 4$) were collected and counted for radioactivity at different time points (Fig. 4A). The [$^{111}$In]us-GO-DOTA showed the maximum excretion compared to the other two samples. Furthermore the samples were analysed by Raman spectroscopy as shown in Fig. 4B. The Raman signature of GO-DOTA was detected in the urine of all three materials, confirming the excretion of the material regardless of the lateral size. Pooled faecal samples were collected after 24 h and measured for radioactivity, all samples indicated faecal excretion (Fig. 4C).

### 2.6. Histopathology after i.v. administration of the three materials

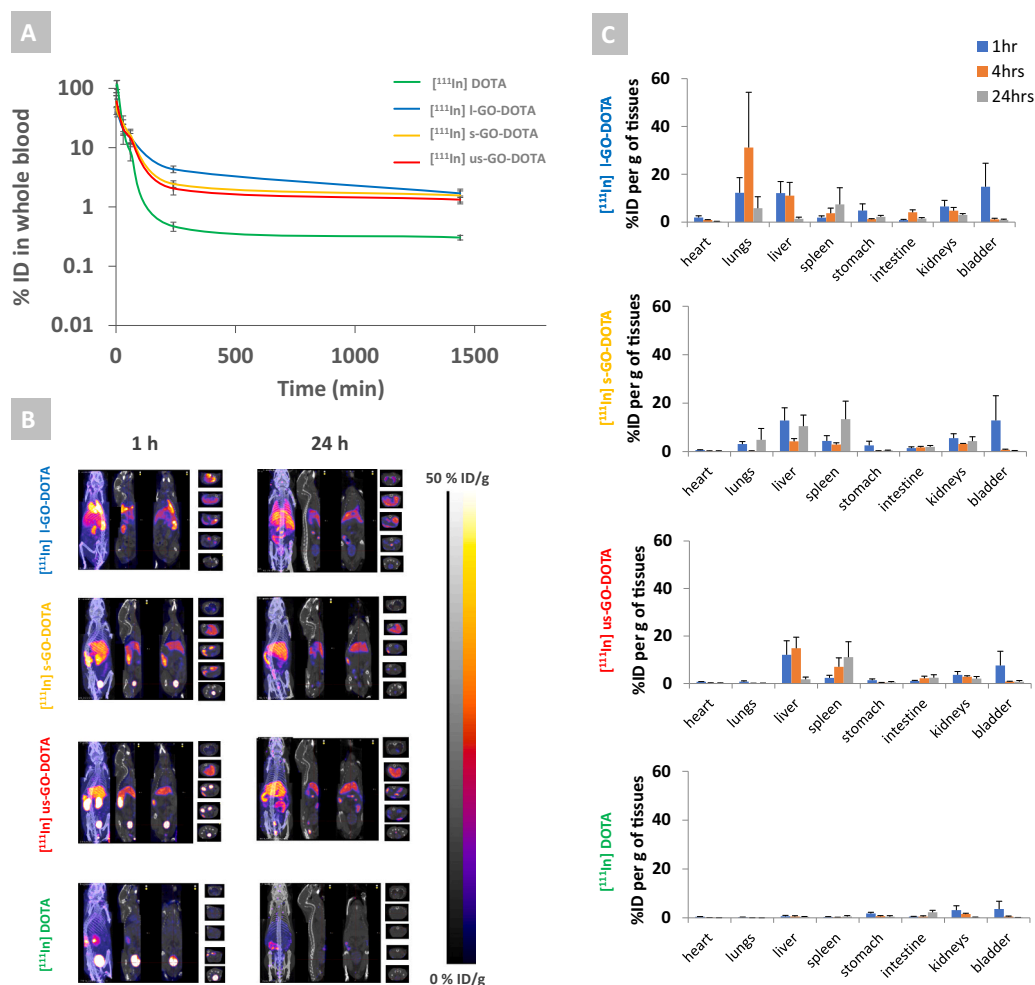Tissue samples (lung, liver, spleen and kidneys) were examined for

**Fig. 3.** Biodistribution of the three types of GO ([$^{111}$In] l-GO-DOTA, [$^{111}$In] s-GO-DOTA and [$^{111}$In] us-GO-DOTA) compared to [$^{111}$In]DOTA control at 1 h and 24 h. A) Blood profile up to 24 h. B) SPECT/CT images expressed as % of injected dose per gram of tissues (doses were decay corrected at the second time point). From left to right (whole body maximum intensity projections (MIP), sagittal, coronal and transverse views). Interactive 3D images of the MIPs are available online. C) Organ distribution of the three materials as determined by γ-counting. Four animals per group were used for A and C, while two animals were used for the imaging in (B).

histopathology using H & E (haematoxylin and eosin) staining of paraffin embedded tissue sections for two animals per condition (Fig. 5 and Figs. S10–15). Lungs of mice injected with all the GO materials demonstrated an interesting distribution pattern (Fig. 5 and Fig. S10). All GO materials were predominantly detected as agglomerates within the lumen of lung blood vessels, which indicates the retention of GO in the lung capillaries as a size-dependent phenomenon, with the l-GO-DOTA material showing the largest, and the most agglomerates, as quantified in Fig. S11 and shown in different regions in Fig. 5 and Fig. S10. In the case of the mice spleen samples, no evidence of histopathology was determined in the red pulp (second panel) and the white pulp (third panel) in any of the samples as compared to the controls (Figs. S12–13). Liver tissue (Fig. S14) and kidney tissue (both glomerular and tubular regions) (Fig. S15) also demonstrated healthy anatomical structures with no evident histopathology in any of the samples.

## 3. Discussion

To date there is no direct method to quantitatively measure the amount of GO in physiological fluids (e.g. tissues, blood and urine) due to the background interferences from the complex molecular composition of such biological fluids. Studies rely on labelling of the material for quantification, though other methods can offer qualitative detection such as TEM and Raman spectroscopy. In this work, we studied the pharmacokinetic profile of three lateral sizes of thin GO sheets. The functionalisation of GO with PEGylated DOTA was performed to allow the chelation of a radioactive metal [$^{111}$In] for studying and quantifying

the tissue distribution of the materials. The functionalisation of GO with the PEGylated DOTA was performed via epoxide opening. Because of the abundance of epoxides on the GO surface, this strategy generally leads to higher levels of functionalization compared to the derivatisation of hydroxyls or carboxylic acids [47].

Structural characterisation was carried out by TEM and AFM to reveal whether GO sheets would have marked differences in their morphology. The materials were produced with controlled lateral dimensions by tuning their lateral size by sonication as previously reported [37,48–50]. After functionalization all three materials maintained their 2D morphology, while the thickness increased from single to a few layers following DOTA functionalization due to the presence of the functional groups and minor agglomeration that led to slightly thicker sheets. These findings are consistent with previous reports of functionalization of GO with DOTA [27,28] PEG [20,51], dextran [25] and bovine serum albumin [52]. Interestingly, we noticed that l-GO underwent a marked reduction in sheet lateral dimension after DOTA functionalization. Surface functionalization of GO has also been reported to reduce the lateral dimension of the sheets [28,52]. However, the lateral dimensions of all functionalized GO-DOTA materials remained markedly different from each other.

The analysis of the XPS spectra (Table S1 and Figs. S1–3) showed that the functionalization of GO with the DOTA derivative was successful, as demonstrated by the detection of nitrogen in the GO-DOTA materials compared to their starting counterparts. Moreover, nitrogen atoms were detected in the form of amines and amides (Fig. S3), which are present in the DOTA molecule. The higher intensity of the carbonyl peak in the carbon high resolution spectra after functionalization (Fig. S1) is due to
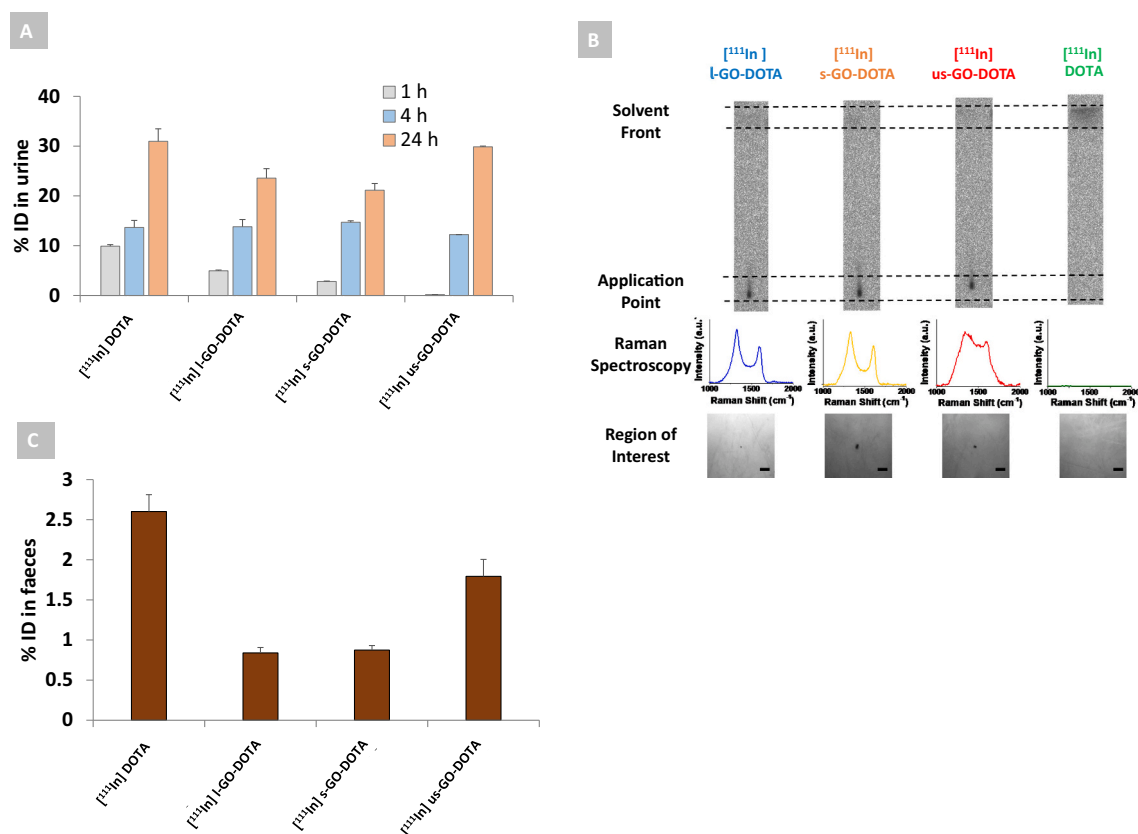
**Fig. 4.** Excretion profile of l-, s- and us-GO ([111In]l-GO-DOTA, [111In]s-GO-DOTA and [111In]us-GO-DOTA) compared to control [111In]DOTA. A) Urinary excretion profile of the three materials at different time points; B) detection of the graphene material in the urine 24 h post administration of mice as demonstrated by radio-TLC and corroborative Raman spectroscopy (scale bars are 20 μm); C) faecal excretion of the three materials compared to the control.

the carboxylic acids of the DOTA molecule and it is also an indication of the presence of amides. On the other hand, the changes in the carbon high resolution spectra after functionalization are more subtle. First, there is a decreased abundance of oxidised carbon atoms compared to the graphitic carbon region, due to the loss of some labile groups after functionalization of GO. The contribution of the epoxides (C-O-C) is reduced compared to the C-OH/C-N band, which is coherent with the introduction of the DOTA moiety by opening of epoxides, thus generating C-OH and introducing amino groups. Chemical functionalization of GO was further evidenced by analysing the different GO derivatives by TGA under an inert atmosphere (Fig. S4). GO is thermally unstable and starts to lose mass at temperatures even lower than 100 °C due to residual water molecules adsorbed on the GO sheets. A main weight loss was identified at 230 °C that is due to the elimination of labile oxygen-containing groups [53]. All GO-DOTA materials revealed a lower thermal stability probably due to functionalization with DOTA. Therefore, taken together these results confirm the effective grafting of DOTA on the surface of the three GO samples. In addition, the structure of GO is preserved and the functionalization strategy induced no significant reduction, thus enabling to obtain stable suspensions in aqueous solutions.

Other studies have reported radiolabelling of GO materials with iodine resulting in iodinated constructs that are unstable, while the high affinity of iodine for the thyroid gland can be misleading with regards to 2D material biodistribution profiles [25]. Radiolabelling with $^{111}$In has been performed previously using physical adsorption of the DTPA (diethylenetriaminepentaacetic acid) chelating agent on the surface of GO by π-stacking. Such strategy however increased the thickness of the GO sheets dramatically [33]. The radiolabelling efficiency and stability of covalently bound DOTA to GO materials has been tested before with high efficiency and stability [27,28]. In this study a similar strategy was

exploited using GO materials with three different lateral dimensions (l-GO-DOTA, s-GO-DOTA and us-GO-DOTA). The radiolabelling efficiency was not affected dramatically by the lateral size of the GO sheets. All samples remained stable up to 24 h at 37 °C in 50% serum. Similar to original samples without serum incubation, the control [111In]DOTA travelled to the solvent front as compared to the three samples that remained at the bottom of the TLC (Fig. S5). This indicated that the [111In]DOTA was attached to the GO materials with no interferences occurring from the serum proteins at the times that were tested (reflecting the time predicted for the material will spend in blood after injection and beyond that time). This avoids any possible conflictions in the tissue distribution that are created from the detachment of the [111In]DOTA. Therefore the purity of material was confirmed to be suitable for in vivo administration. Furthermore the in vivo stability was confirmed by the Raman signal that coregistered with the radioactivity at the bottom of the TLC strips in the urine of the mice after injection as compared to the control free label that was predominantly at the top of the TLC strips (Fig. 4B). This was comparable to the original samples before injection in Fig. 2B this further confirmed the stability and association of the label with the GO material even after injection.

Compared to our previous studies [27–29] where the small and thin GO-DOTA material was only injected, in this study, three materials with comparable thickness and the three different sizes were injected intravenously in mice. All three materials were removed from blood within minutes, as shown by the first-phase distribution half-life ($t_{1/2\alpha}$). Although no significant differences were seen in the pharmacokinetic data of the materials, the [111In]DOTA control was removed from blood faster. In the second phase the [111In]us-GO-DOTA material was more similar to [111In]DOTA control and remained slightly longer in circulation in the second phase half-life ($t_{1/2\beta}$). The amounts remaining in blood after 1 h and 24 h were more elevated for the [111In]s-GO-DOTA
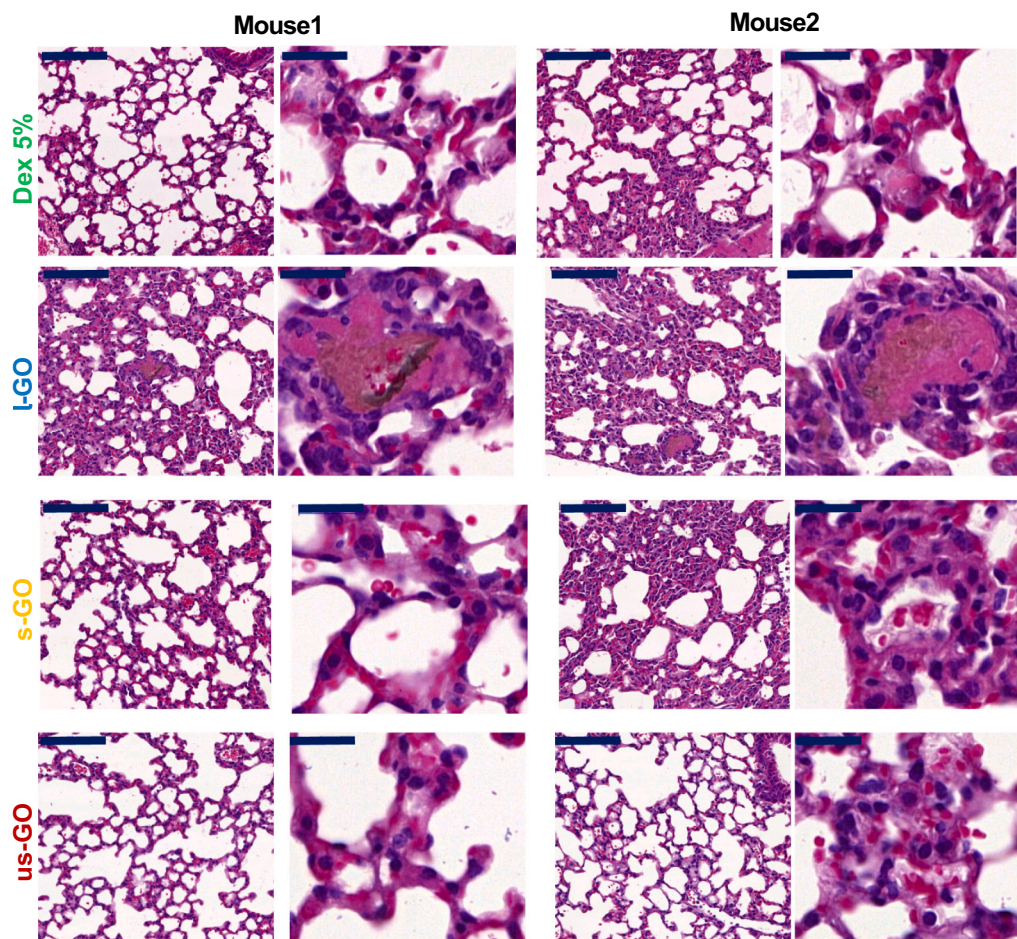
**Fig. 5.** Effect of non-radiolabelled l-GO-DOTA, s-GO-DOTA, us-GO-DOTA on lung compared to vehicle alone (5% dextrose). Haematoxylin and eosin stained lung sections (5 μm thick) after injection of l-GO-DOTA, s-GO-DOTA, us-GO-DOTA and 5% dextrose (negative control) after 24 h of two different mice for each material. Two magnifications were used, with scale bars on the left in each panel showing 100 μm, while those on the right are indicating 20 μm.

and [111In]us-GO-DOTA compared to [111In]l-GO-DOTA (Fig. 3A, Fig. S5,Table S2 and Table S3). Smaller nanoparticles are well known to circulate longer [54,55].The area under the blood concentration time curve (AUC), steady state volume of distributions (Vd$_{ss}$) (indicating the body overall and tissue exposure) and the clearance values are shown in Table S2. The [111In]DOTA control was almost entirely removed from blood at the early hours after administration (Table S3). On the contrary, the remaining amounts in the whole body after 24 h for the three materials was much higher compared to control material (Table S4).

It is clear from our results that tissue distribution occurs very rapidly for all three materials and is largely affected by the size of the graphene sheet (Fig. 3B-C and Figs. S6–9). It is very evident that the large material ([111In]l-GO-DOTA) tends to accumulate in the lungs early after injection, with reductions in the signal after 24 h as seen by both the time activity curve and the γ-counting experiment (Fig. S7 and Fig. 3C, respectively). Larger nanomaterials tend to accumulate in the lungs after i.v. administration due to the first capillary bed [55]. This has also been demonstrated with graphene materials [17,56,57]. Some material also remained in the lung tissues after 24 h as seen in the SPECT/CT data, γ-counting and in the H & E sections/semi-quantification (Fig. 3B-C, Figs. S6–9 and S11). Some thickening of the alveolar walls was also seen especially in lungs from mice injected with l-GO-DOTA and s-GO-DOTA, indicating cellular infiltration and constriction, probably as a result of the material entrapment in the lung tissues. We observed a clear reduction of the lung signal after 24 h. It is known that the removal of nanomaterials from the lung is carried out by phagocytic uptake of the lung macrophages. This is the main mechanism to remove the insoluble

aggregated nanoparticles into the micrometer-sized particles from the lung tissues. Particle-containing macrophages may re-enter into the interstitium and be cleared by the lymphatics or other organs [58].

The smaller materials ([111In]s-GO-DOTA and [111In]us-GO-DOTA) accumulated mainly in the liver and spleen with slight variability between animals in maximum accumulations in these organs. The [111In] us-GO-DOTA showed a slight reduction in the hepatic signal after 24 h compared to the [111In]s-GO-DOTA that remained the same. On the other hand, both materials accumulated in the spleen at high concentration even after 24 h (Fig. 3B-C and Figs. S6–9). It is well known that nanomaterials, including graphene-based materials, get trapped in the mononuclear phagocytic system (RES) [16,25,34,59,60]. This happens within the liver due to the non-continuous liver endothelia with vascular fenestrations measuring 50–100 nm, leading to nonspecific accumulation of nanoparticles within this range. In the spleen, interendothelial cell slits with a size range of 200–500 nm mediate the retention of particles >200 nm [55]. Particle shape also accounts for accumulation in certain tissues, with elongated nanoparticles mainly in the spleen, while the more spherical ones accumulate in the liver [61]. The total amount of material remaining in the body of mice injected with the [111In]l-GO-DOTA was the highest compared to the other two materials (Table S3), which can be explained by the fact that larger and thicker materials are more difficult to be cleared from the body [27].

Though there was slight variability between animals, the bladder measurements obtained from the γ-counting experiments are largely dependent on the urine content in the bladder that can largely vary. But, it is clear from the data obtained herein that the graphene sheets were

excreted through urine regardless of their lateral dimension (Figs. 3B-C, 4A-B, Figs. S6–9). The Raman signature of GO-DOTA was detected in the urine of injected mice confirmed the presence of intact sheets undergoing urinary excretion. The kidney and bladder profiles in Fig. 3B-C and Fig. S6 suggested that the larger sheets ([111In]l-GO-DOTA) were excreted at a slower rates compared to the other two materials ([111In]s-GO-DOTA and [111In]us-GO-DOTA). Though, there could be a possibility of a very small fraction of small sheets in all the three GO-DOTA samples because of population of size distributions, however previous studies by our group and others gave direct evidence of the excretion of much larger sheets than the kidney glomerular filtration cut off due to their thin and flexible nature [29,62]. All materials had a delayed excretion profile compared to the control probe, which was eliminated almost entirely instantly. Gamma counting of pooled urine samples can sometimes be misleading due to huge loss on the surfaces of the metabolic cages. Therefore, comparing the quantities in urine to the control ([111In]DOTA) chelator sample is more realistic as the chelating agents are predicted to be excreted almost entirely with minimal tissue accumulation [63]. We observed that the quantities excreted were much higher for the us-GO-DOTA compared to the other two samples ([111In]l-GO-DOTA and [111In]s-GO-DOTA) and close to the excretion of the control [111In]DOTA. Overall, these results show that all three materials were excreted and the smaller material was excreted faster and to a larger extent.

We and others have demonstrated previously that large, thin functionalized GO sheets can cross the glomerular filtration barrier (GFB) although they have dimensions that exceed the GFB cut off [16,27–29,62]. However, this is the first time we demonstrate urinary excretion of large GO sheets. Our histological data (Fig. S16) resonates with our previous results, illustrating the lack of damage to kidney regions. This suggested that excretion of GO sheets occurred as a passive mechanism regardless of their size (provided they are thin and flexible enough), possibly due to their morphological reconfiguration of the sheets either by sliding, squeezing, rolling or folding [29].

The small intestinal signals in the SPECT/CT images at 24 h and values in faeces suggested slight faecal excretion, which could occur by biliary excretion, similarly to previous findings with PEGylated GO [16], which bared PEG moieties functionalized GO-DOTA materials. No damage to organs (spleen, liver and kidneys) was determined by our histological H & E examinations for all three materials, consistent with many other previous studies [16,20,64,65]. However, lung sections indicated some thickening of the alveolar walls especially for the large material (Fig. 5, S11–12). All three GO-DOTA materials were detected as agglomerates within the lumen of the lung blood vessels (Fig. S12) and the retention of material in the lung capillaries was a size-dependent phenomenon. This retention and lung histopathological changes that can further lead to fibrosis and lung damage at later time points have been observed in other studies using large and non-functionalized materials [56,66,67] and requires further investigations.

In conclusion, GO was successfully covalently functionalized with the PEGylated DOTA chelator with high chemical and radiolabelling stability regardless of the GO starting lateral dimension. Intravenous administration of the GO-DOTA constructs led to rapid and significant uptake by the lungs of the larger material, while the smaller materials targeted the liver and spleen. All three radiolabelled GO-DOTA materials were excreted regardless of their lateral dimension, indicating the possibility that the thickness rather than size may be the major factor that governs the ability of GO to be excreted. Nevertheless, the lateral dimension affected the rate of excretion. These findings provide further insight on the kinetics and biodistribution of thin functionalized GO sheets with different lateral dimensions after intravenous administration in mice. This has important implications in the future design of graphene-based materials for biological applications and for targeting of different organs. Indeed, large GO could be exploited for lung delivery, whereas smaller dimensions could target the liver and spleen. Ultra-small GO is excreted to a larger extent, which would make it

attractive for imaging applications such as dynamic imaging where the contrast agent needs to exit the body quickly after the imaging session [68]. Due to high surface area they could further be used to deliver imaging probes and therapeutics simultaneously for theranostic applications. Future studies are necessary to further assess the long-term safety profile from repeated accumulations of graphene-based nanomaterials and warrant direct quantitative detection techniques of the materials in the tissue enviorment in which they will reside for further validation.

## 4. Experimental

### 4.1. Chemical synthesis of GO

All reagents used in the production of GO were purchased from Sigma Aldrich (UK), except water for injections, which was obtained from Dutscher Scientific (UK). GO was produced by a modified Hummers' method under endotoxin-free conditions [35–37]. All glassware were depyrogenated prior adding the mixture of 0.8 g of graphite flakes (Graflake 9580, kindly provided by Nacional de Grafite Ltda, Brazil) with 0.4 g of sodium nitrate in a round-bottom flask that was placed in an ice bath, followed by the slow addition of 18.4 mL of 99.999% sulphuric acid. When the mixture became homogenised, 2.4 g of potassium permanganate was slowly added for 30 min. The dropwise addition of 37.5 mL of water for injections resulted in a violent exothermic reaction, after which the temperature of the mixture was carefully maintained at 98 °C for 30 min. After the addition of 112.5 mL of water for injection, the reaction was stopped with 12 mL of 30% hydrogen peroxide, which reduced the unreacted potassium permanganate and manganese-based intermediate products to manganese sulphate salts. The resulting graphite oxide suspension underwent a series of exfoliation and centrifugation steps at 9000 rpm for 20 min, where the supernatant was replaced by fresh water for injections, until the pH of the supernatant became neutral and a brownish gel-like layer was formed on the top of the pellet. Warm water for injections was used to extract l-GO flakes from the graphite pellet. In order to produce s-GO flakes, l-GO underwent a 5-min sonication step in a bath sonicator (VWR, UK) operating at 80 W, which exfoliated and broke down the micrometer-sized flakes. The exfoliated suspensions were centrifuged at 13000 rpm for 20 min at 20 °C, and the respective supernatants were carefully extracted, containing only the small nanometre-sized flakes. For production of the us-GO flakes, the l-GO underwent a similar process, involving a 4-h sonication step followed by centrifugation at 13000 rpm for 1 h at 20 °C.

### 4.2. Preparation of GO-DOTA materials

NH$_2$-PEG$_4$-DOTA (CheMatech) (9 mg, 0.0129 mmol) was added to an aqueous suspension of GO starting materials (us-GO, s-GO or l-GO) (9 mg, 1 mg/mL). The mixture was left to react for 2 days under continuous stirring at room temperature. GO-DOTA was then directly dialyzed in MilliQ water for 4 days. The final dialyzed GO-DOTA was stored at 7 °C in water without further treatment.

### 4.3. Preparation of $^{111}$In labeled GO-DOTA and control DOTA materials

l-GO-DOTA, s-GO-DOTA, us-GO-DOTA and control material DOTA (PEG)$_4$-NH$_2$ referred in this manuscript as 'DOTA' for ease, were diluted with an equal volume of 0.2 M ammonium acetate buffer pH 5.5, to which 10–20 MBq of $^{111}$InCl$_3$ (CURIUM™ previously, Mallinckrodt RP) was added, in separate experiments. The indium was left to react with the GO-DOTA and DOTA control for 60 min at 60 °C with vortexing every 5 min after which the reaction was quenched by the addition of 0.1 M EDTA chelating solution. The radiolabelling was carried out in several separate experiments at different occasions and with different operators.

### 4.4. Radiolabelling efficiency of GO-DOTA materials

To determine the labelling efficiency of each final product, aliquots were diluted five folds in PBS and then 1 μL spotted on silica gel impregnated glass fibre sheets (PALL Life Sciences, UK). The strips were developed with a mobile phase of 25 mM EDTA in 0.1 M ammonium acetate and allowed to dry before analysis. This was then developed and the autoradioactivity counted using a Fujifilm fluorescence image analyser (FLA-3000 series, Tokyo, Japan). The immobile spot on the TLC strips indicated the percentage of radiolabeled GO-DOTA, while free [111In]DOTA(PEG)4-NH2, referred throughout this manuscript as [111In]DOTA for ease was seen as the mobile spots near the solvent front.

### 4.5. Radiolabelling stability of GO-DOTA materials

To determine the stability of the labeled [111In]GO-DOTA materials, aliquots of each final product were diluted five-fold either in PBS or 50% mouse serum and then incubated at 37 °C over 1 week. At different time points (0 h, 24 h, 48 h and 7 days), 1 μL of the aliquots was spotted on silica gel impregnated glass fibre sheets and then developed, and quantified as described above.

### 4.6. TEM analysis

20 μL of sample (200 μg/mL) was dropped on a glow-discharged carbon-coated copper grid (CF400-Cu) (Electron Microscopy Services, UK). Filter paper (Merck-Millipore, UK) was used to absorb the unbound material. Samples were then observed with a FEI Tecnai 12 BioTWIN microscope (Techni, Netherlands) with an acceleration voltage of 100 kV. Images were taken using a Gatan Orius SC1000 CCD camera (GATAN, UK). Size using TEM distributions were performed as described previously [37,49,50].

### 4.7. AFM analysis

AFM was performed on freshly cleaved mica, treated with 40 μL of poly-L-lysine (Sigma-Aldrich, UK) to present a positively charged surface, which facilitated the adhesion of the GO sheets. Aliquots of 10 μL were then transferred of the respective suspensions onto the mica surface coated with poly-L-lysine and left to adsorb for 2 min. Unbound GO sheets were then removed via gentle washing with 2 mL of MilliQ $H_2O$ and left to dry at room temperature. During analysis, a Multimode atomic force microscopy (Bruker, UK) was used in tapping mode in order to reduce damage to the samples for height (trace and retrace) and amplitude. Scans were completed using an Otespa tapping mode tip (Bruker, UK) using the following parameters: a scan rate of 1 Hz; lines per scan of 512; an integral gain of 1 and a proportional gain of 5; an amplitude set point value of 150 mV was maintained constant between all measurements. Scan areas were set at 2500 μm², 400 μm², 100 μm², and 25 μm². Post image processing was completed using the Bruker Nanoscope Analysis software (version 1.4, Bruker, UK). Size and thickness distributions were performed as described previously [37,49,50].

### 4.8. XPS analysis

The three GO-DOTA aqueous suspensions were drop-casted on silicon wafers and dried overnight. XPS analysis was carried out with a Thermo Scientific K-ALPHA monochromatic photoelectron spectrometer with a basic chamber pressure of $10^{-8}$–$10^{-9}$ bar and an Al anode as X-ray source (1486 eV). A spot size of 400 μm was selected. Every sample was analysed three times. The survey spectra are an average of 10 scans taken with a pass energy of 200.00 eV and a step size of 1 eV. The high resolution spectra are an average of 10 scans taken with a pass energy of 50.00 eV and a step size of 0.1 eV. The pass energy of 50.00 eV corresponds to Ag $3d_{5/2}$ line FWHM of 1.3 eV. A pass energy of 50.00 eV for the high resolution spectra was applied because using lower pass

energies has shown no improvement in FWHM for graphene materials on Thermo Scientific K-ALPHA. An electron flood gun was turned on during analysis as charge neutralizer. This electron flood gun was not totally efficient for charge compensation, thus an error due to charging was still identified in some samples.

Data analysis casaXPS (2.3.18) software was used. A Shirley background subtraction and charge correction were applied. No reference element was analysed, thus, the spectra were corrected to the C—C peak at 285.2–285.3 eV, if needed. Error due to this charge correction was taken into account. A line-shape 70% Gaussian/30% Lorenzian [GL [30]] is selected for all peaks beside for $sp^2$ C peak. For $sp^2$ C peak an asymmetric line-shape was chosen [A(0.4, 0.38, 20)GL [20]]. FWHM was constrained to be the same for all peaks, beside the pi-pi* peak and the water peak because these are broad signals. The peak position for each bond was constrained to be the same in every spectra, with a low ratio of variability. Due to the difficulty to take standards for carbon nanomaterials, database and reference articles were used as peak reference value. For the carbon high resolution spectra almost every bond was considered individually, keeping into consideration the error due to the proximity of the binding energy (BE) values and proportional to the overlapping ratio. Only C-OH/C-N and C=OOH/C=ONR₂ were cumulated under the same peak due to the higher proximity of the BE values. For oxygen and nitrogen high resolution spectra all signals were assembled due to the high proximity of the BE values instead. Also with this approximation a certain degree of error has to be taken into account [69–71].

### 4.9. Thermogravimetric analysis

TGA was performed using a TGA1 (Mettler Toledo) apparatus from 30 °C to 900 °C with a ramp of 10 °C/min under $N_2$ using a flow rate of 50 mL/min and platinum pans.

### 4.10. Raman spectroscopy of GO, GO-DOTA samples in solution and GO-DOTA samples in urine

Samples were prepared for analysis via drop casting 20 μL of GO (100 μg/mL) dispersion onto a glass slide. Samples were left to dry for at least 2 h at 37 °C. For the identification of GO in the urine, 5 μL of collected urine were spotted on new silica gel impregnated glass fibre sheets and then developed as described above. The developed TCL plates were then left for radioactivity decay for a month. The application points on each TCL plate were screened for GO using Raman spectroscopy. As Raman is a qualitative method of detection and urine components prove to be masking the GO signal at low concentrations, the 24 h collected urine was only chosen where there was the maximum amount of GO excreted for facilitating the detection of the signal.

Spectra were acquired using a micro-Raman spectrometer (Thermo Scientific, UK) using a $\lambda = 633$ nm laser at 0.4 mW with an exposure time of 25 s at a magnification of $50\times$. Spectra were averaged over 5 locations and considered between 500 and 3500 $cm^{-1}$. Post spectral processing included background correction and baseline subtraction, followed by the calculation of the I(D)/I(G) intensity ratio, this was completed using OriginProsoftware (version 8.5.1, Origin Lab, USA).

### 4.11. Animal handling procedures

Six- to eight-week-old C57BL6 mice (18.7 ± 2.4 g) were obtained from Envigo (ex-Harlan) (Oxfordshire, UK), allowed to acclimatize for 1 week and were given access to food and water for the duration of the experiments. All procedures were carried out in accordance with the UK Home Office Code of Practice (1989) for the housing and care of animals in scientific procedures, in accordance with prior approval from the UK Home Office. All mice were injected with a single injection of either l-GO, s-GO, us-GO, l-GO-DOTA, s-GO-DOTA or us-GO-DOTA (2.5 mg/kg) or control materials such as dextrose 5% or [111In]DOTA in 200 μL by

either i.v. bolus injection or infusion through the tail vein.

## 4.12. SPECT/CT

Mice were subjected to anaesthesia via the inhalation of 2.5% isoflurane where oxygen was used as a carrier gas set at a flow rate of 2 L/min. Each animal was then intravenously injected with the radioactive materials (either [$^{111}$In]l-GO-DOTA, [$^{111}$In]s-GO-DOTA, [$^{111}$In]us-GO-DOTA or [$^{111}$In]DOTA) at a dose of 2.5 mg/kg (200 μL, 5–10 MBq). The injections were carried out by i.v. infusions through tail vein catheterisation in order to enable the dynamic imaging. At 0-1 h and 24 h SPECT/CT imaging was carried out using a Nano-Scan® SPECT/CT scanner (Mediso, Hungary). SPECT images were obtained in 20 projections over 40–60 min using a 4-head scanner with 1.4 mm pinhole collimators for the 3D pinSPECT images and a custom made 3 mm single pinhole collimator for the dynamic (time laps) and static 2D images. Due to practicalities of radioisotope decay and large number of samples tested it was decided to run the fast 2D static scan at the mid-point 4 h time point rather than the full 3D pinSPECT scans that take much longer time. CT scans were taken at the end of each SPECT acquisition using a semi-circular method with full scan, 480 projections, maximum FOV, 35 kV energy, 300 ms exposure time and 1–4 binning. Acquisitions were done using the Nucline v2.01 (Build 020.0000) software (Mediso, Hungary), while reconstruction of all images and fusion of SPECT with CT images was performed using the Interview™ FUSION bulletin software (Mediso, Hungary). The images were further analysed using VivoQuant 3.0 software (Boston, US) where the SPECT images with scale bars in MBq were corrected for decay and for the slight differences in radioactivity in the injected doses between animals. Images containing scale bars in %ID per gram were processed automatically by the VivoQuant software after providing the injected dose in MBq.

## 4.13. Gamma scintigraphy

For more quantitative assessment of tissue biodistribution, a cut and count study was carried out. Mice were anaesthetised by isoflurane inhalation. Each animal was injected in the tail vein with one of the radiolabelled constructs either [$^{111}$In]l-GO-DOTA, [$^{111}$In]s-GO-DOTA, [$^{111}$In]us-GO-DOTA or [$^{111}$In]DOTA 200 μL containing 2.5 mg/kg containing approximately 5–10 MBq. Mice were sacrificed at 1, 4 and 24 h after injection. Blood and all major organs and tissues were collected including, heart, lungs, liver, spleen, stomach, intestine, kidneys, and bladder. Urine and faeces were pooled and collected as well. Each sample was weighted and counted on a γ-counter (Perkin Elmer, USA), together with a dilution of the injected dose with dead time limit below 60%. The percentage injected dose per gram tissue was calculated, using four different mice for each time point.

## 4.14. Histological analysis

Lungs, liver, spleen and kidneys were extracted from mice after 24 h and fixed with 4% paraformaldehyde. This was followed by paraffin embedding of sections at known orientations. Sections of 5 μm were stained with H & E and imaged using a 3D Histech Pannoramic 250 Flash slide scanner. Images were processed and analysed using Pannoramic Viewer (http://www.3dhistech.com/) and Fiji/ImageJ software (version 1.5c; National Institutes of Health, Bethesda, MD).

## 4.15. Statistical analysis

Due to different sample sizes and the non-Gaussian distribution of the flake populations, the TEM size distribution data were presented using boxplots and the median, minimum and maximum values of each distribution were reported. A non-parametric test (Wilcoxon rank sum test) was performed using the statistical package in MATLAB (version R2013a, MathWorks Inc., USA), in order to determine the statistical significance of the difference between the lateral dimensions of the GO materials. Experiments were completed with an $n = 3$–4 repeats and values are mean ± standard deviation (SD). Animal experiments were completed with at least two repeats for each imaging and histological experiments and $n = 4$ repeats for the quantitative experiments and values are mean ± standard error of the mean (SEM). One-way ANOVA with Tukey's posthoc test using IBM SPSS statistics 25 software were used when considering multiple comparisons for the pharmacokinetic data.

## Author contributions

D.J. designed, planned, and led the study, performing all of the animal experiments, imaging, histopathology, radiolabelling studies and data analysis, prepared the figures and wrote the manuscript. L.N. contributed to the characterisation of GO and GO-DOTA using TEM and AFM. He performed the Raman spectroscopy experiments and helped perform the radiolabelling experiments. A.R. and N.L. prepared the initial GO and performed the physicochemical characterisation of GO and GO-DOTA samples. A.R. also helped analyse the lung histopathology data. I.V. and M. L.. performed the chemical functionalisation of GO with DOTA and performed the XPS and TGA experiments and analysis. C.M. designed and supervised the chemical reaction of GO with DOTA. A.B. provided continuous guidance in the conceptual design of the work and data interpretation. K.K. designed, planned, and discussed the findings, reviewed and edited the manuscript, and overall supervised the work. D.J., L.N., A.R., I.V., M. L., C.M., A.B. and K.K. discussed the findings and contributed to writing, reviewing, and editing the manuscript.

## References

[1] K. Kostarelos, K.S. Novoselov, Graphene devices for life, Nat. Nanotechnol. 9 (2014) 744.

[2] Y. Pan, N.G. Sahoo, N. Li, The application of graphene oxide in drug delivery, Expert Opin. Drug Deliv. 9 (2012) 1365–1376.

[3] P. Avouris, F. Xia, Graphene applications in electronics and photonics, MRS Bull. 37 (2012) 1225–1234.

[4] Z. Liu, J.T. Robinson, X. Sun, H. Dai, PEGylated nanographene oxide for delivery of water-insoluble cancer drugs, J. Am. Chem. Soc. 130 (2008) 10876–10877.

[5] K. Kostarelos, K.S. Novoselov, Exploring the interface of graphene and biology, Science 344 (2014) 261–263.

[6] K.P. Loh, Q. Bao, G. Eda, M. Chhowalla, Graphene oxide as a chemically tunable platform for optical applications, Nat. Chem. 2 (2010) 1015–1024.

[7] L. Feng, Z. Liu, Graphene in biomedicine: opportunities and challenges, Nanomedicine 6 (2011) 317–324.

[8] H. Shen, L. Zhang, M. Liu, Z. Zhang, Biomedical applications of graphene, Theranostics 2 (2012) 283–294.

[9] I. Calizo, I. Bejenari, M. Rahman, G. Liu, A.A. Balandin, Ultraviolet Raman microscopy of single and multilayer graphene, J. Appl. Phys. 106 (2009), 043509.

[10] A.C. Ferrari, et al., Raman spectrum of graphene and graphene layers, Phys. Rev. Lett. 97 (2006) 187401.

[11] A. Bendali, et al., Purified neurons can survive on peptide-free graphene layers, Adv. Healthc. Mater. (2013) 929–933.

[12] K.S. Novoselov, et al., A roadmap for graphene, Nature 490 (2012) 192–200.

[13] M. Zhou, et al., Graphene oxide: a growth factor delivery carrier to enhance chondrogenic differentiation of human mesenchymal stem cells in 3D hydrogels, Acta Biomater. 96 (2019) 271–280.

[14] N.A. Kotov, et al., Nanomaterials for neural interfaces, Adv. Mater. 21 (2009) 3970–4004.

[15] S.K. Seidlits, J.Y. Lee, C.E. Schmidt, Nanostructured scaffolds for neural applications, Nanomedicine (London, England) 3 (2008) 183–199.

[16] K. Yang, et al., In vivo pharmacokinetics, long-term biodistribution, and toxicology of PEGylated graphene in mice, ACS Nano 5 (2011) 516–522.

[17] J.H. Liu, et al., Effect of size and dose on the biodistribution of graphene oxide in mice, Nanomedicine (London, England) 7 (2012) 1801–1812.

[18] L. Zhan, et al., Biodistribution of co-exposure to multi-walled carbon nanotubes and graphene oxide nanoplatelets radiotracers, J. Nanopart. Res. 13 (2011) 2939–2947.

[19] G. Qu, et al., The ex vivo and in vivo biological performances of graphene oxide and the impact of surfactant on graphene oxide's biocompatibility, J. Environ. Sci. 25 (2013) 873–881.

[20] K. Yang, et al., In vivo biodistribution and toxicology of functionalized nano-graphene oxide in mice after oral and intraperitoneal administration, Biomaterials 34 (2013) 2787–2795.

[21] L. Yan, et al., Can graphene oxide cause damage to eyesight? Chem. Res. Toxicol. 25 (2012) 1265–1270.

[22] C.M. Girish, A. Sasidharan, G.S. Gowd, S. Nair, M. Koyakutty, Confocal Raman imaging study showing macrophage mediated biodegradation of graphene in vivo, Adv. Healthc. Mater. 2 (2013) 1489–1500.

[23] K. Wang, et al., Biocompatibility of graphene oxide, Nanoscale Res. Lett. 6 (2011), 8–8.

[24] X. Zhang, et al., Distribution and biocompatibility studies of graphene oxide in mice after intravenous administration, Carbon 49 (2011) 986–995.

[25] S. Zhang, K. Yang, L. Feng, Z. Liu, In vitro and in vivo behaviors of dextran functionalized graphene, Carbon 49 (2011) 4040–4049.

[26] K. Yang, et al., Graphene in mice: ultrahigh in vivo tumor uptake and efficient photothermal therapy, Nano Lett. 10 (2010) 3318–3323.

[27] D.A. Jasim, et al., Thickness of functionalized graphene oxide sheets plays critical role in tissue accumulation and urinary excretion: a pilot PET/CT study, Appl. Mater. Today 4 (2016) 24–30.

[28] D.A. Jasim, C. Menard-Moyon, D. Begin, A. Bianco, K. Kostarelos, Tissue distribution and urinary excretion of intravenously administered chemically functionalized graphene oxide sheets, Chem. Sci. 6 (2015) 3952–3964.

[29] D.A. Jasim, et al., The effects of extensive glomerular filtration of thin graphene oxide sheets on kidney physiology, ACS Nano 10 (2016) 10753–10767.

[30] A. Bianco, Graphene: safe or toxic? The two faces of the medal, Angew. Chem. Int. Ed. 52 (2013) 4986–4997.

[31] P. Wick, et al., Classification Framework for Graphene-Based Materials, Angew. Chem. 53 (30) (2014) 7714–7718, https://doi.org/10.1002/anie.201403335.

[32] R.P. Heaney, Factors influencing the measurement of bioavailability, taking calcium as a model, J. Nutr. 131 (2001) 1344S–1348S.

[33] B. Cornelissen, et al., Nanographene oxide-based radioimmunoconstructs for in vivo targeting and SPECT imaging of HER2-positive tumors, Biomaterials 34 (2013) 1146–1154.

[34] H. Hong, et al., In vivo targeting and imaging of tumor vasculature with radiolabeled, antibody-conjugated nanographene, ACS Nano 6 (2012) 2361–2370.

[35] D.A. Jasim, N. Lozano, K. Kostarelos, Synthesis of few-layered, high-purity graphene oxide sheets from different graphite sources for biology, 2D Materials 3 (2016) 014006.

[36] S.P. Mukherjee, et al., Detection of endotoxin contamination of graphene based materials using the TNF-α expression test and guidelines for endotoxin-free graphene oxide production, PLoS One 11 (2016), e0166816.

[37] A.F. Rodrigues, et al., A blueprint for the synthesis and characterisation of thin graphene oxide with controlled lateral dimensions for biomedicine, 2D Materials 5 (2018) 035020.

[38] S. Bhattacharjee, DLS and zeta potential - what they are and what they are not? J. Control. Release 235 (2016) 337–351.

[39] J.L. Li, et al., Oxygen-driven unzipping of graphitic materials, Phys. Rev. Lett. 96 (2006) 176101.

[40] T. Sun, S. Fabris, Mechanisms for oxidative unzipping and cutting of graphene, Nano Lett. 12 (2012) 17–21.

[41] W. Zhang, et al., Unraveling stress-induced toxicity properties of graphene oxide and the underlying mechanism, Adv. Mater. 24 (2012) 5391–5397.

[42] A.M. Dimiev, L.B. Alemany, J.M. Tour, Graphene oxide. Origin of acidity, its instability in water, and a new dynamic structural model, ACS Nano 7 (2013) 576–588.

[43] S. Eigler, C. Dotzer, A. Hirsch, M. Enzelberger, P. Müller, Formation and decomposition of $CO_2$ intercalated Graphene oxide, Chem. Mater. 24 (2012) 1276–1282.

[44] I.A. Vacchi, C. Spinato, J. Raya, A. Bianco, C. Menard-Moyon, Chemical reactivity of graphene oxide towards amines elucidated by solid-state NMR, Nanoscale 8 (2016) 13714–13721.

[45] S. Stankovich, et al., Synthesis of graphene-based nanosheets via chemical reduction of exfoliated graphite oxide, Carbon 45 (2007) 1558–1565.

[46] J.I. Paredes, S. Villar-Rodil, A. Martínez-Alonso, J.M. Tascón, Graphene oxide dispersions in organic solvents, Langmuir 24 (2008) 10560–10564.

[47] I.A. Vacchi, S. Guo, J. Raya, A. Bianco, C. Ménard-Moyon, Strategies for the controlled covalent double functionalization of graphene oxide, Chem. Eur. J. 26 (2020) 6591–6598.

[48] M. Orecchioni, et al., Molecular and genomic impact of large and small lateral dimension graphene oxide sheets on human immune cells from healthy donors, Adv. Healthc. Mater. 5 (2016) 276–287.

[49] A.F. Rodrigues, et al., Size-dependent pulmonary impact of thin graphene oxide sheets in mice: toward safe-by-design, Adv. Sci. (2021) 1903200, n/a.

[50] L. Newman, et al., Nose-to-brain translocation and cerebral biodegradation of thin graphene oxide nanosheets, Cell Reports Phys. Sci. 1 (2020) 100176.

[51] W. Zhang, et al., Unraveling stress-induced toxicity properties of graphene oxide and the underlying mechanism, Adv. Mater. 24 (2012) 5391–5397.

[52] Y. Li, et al., Surface coating-dependent cytotoxicity and degradation of graphene derivatives: towards the design of non-toxic, degradable nano-graphene, Small (2013) 1544–1554.

[53] I. Jung, et al., Reduction kinetics of graphene oxide determined by electrical transport measurements and temperature programmed desorption, J. Phys. Chem. C 113 (2009) 18480–18486.

[54] F. Alexis, E. Pridgen, L.K. Molnar, O.C. Farokhzad, Factors affecting the clearance and biodistribution of polymeric nanoparticles, Mol. Pharm. 5 (2008) 505–515.

[55] E. Blanco, H. Shen, M. Ferrari, Principles of nanoparticle design for overcoming biological barriers to drug delivery, Nat. Biotechnol. 33 (2015) 941–951.

[56] K. Wang, et al., Biocompatibility of graphene oxide, Nanoscale Res. Lett. 6 (2011) 1–8.

[57] S.K. Singh, et al., Thrombus inducing property of atomically thin graphene oxide sheets, ACS Nano 5 (2011) 4987–4996.

[58] M. Geiser, Update on macrophage clearance of inhaled micro- and nanoparticles, J. Aerosol Med. Pulm. Drug Deliv. 23 (2010) 207–217.

[59] K. Yang, et al., The influence of surface chemistry and size of nanoscale graphene oxide on photothermal therapy of cancer using ultra-low laser power, Biomaterials 33 (2012) 2206–2214.

[60] H. Hong, et al., In vivo targeting and positron emission tomography imaging of tumor vasculature with (66)Ga-labeled nano-graphene, Biomaterials 33 (2012) 4147–4156.

[61] M. Zhang, et al., Radiolabeling, whole-body single photon emission computed tomography/computed tomography imaging, and pharmacokinetics of carbon nanohorns in mice, Int. J. Nanomedicine 11 (2016) 3317–3330.

[62] S. Liang, et al., In vivo pharmacokinetics, transfer and clearance study of graphene oxide by La/Ce dual elemental labelling method, NanoImpact 17 (2020) 100213.

[63] B.T. Kurien, N.E. Everds, R.H. Scofield, Experimental animal urine collection: a review, Lab. Anim. 38 (2004) 333–361.

[64] B. Li, et al., Influence of polyethylene glycol coating on biodistribution and toxicity of nanoscale graphene oxide in mice after intravenous injection, Int. J. Nanomedicine 9 (2014) 4697–4707.

[65] L. Newman, et al., Splenic capture and in vivo intracellular biodegradation of biological-grade graphene oxide sheets, ACS Nano 14 (2020) 10168–10186.

[66] M.C. Duch, et al., Minimizing oxidation and stable Nanoscale dispersion improves the biocompatibility of Graphene in the lung, Nano Lett. 11 (2011) 5201–5207.

[67] L. Ma-Hock, et al., Comparative inhalation toxicity of multi-wall carbon nanotubes, graphene, graphite nanoplatelets and low surface carbon black, Part. Fibre Toxicol. 10 (2013) 23.

[68] S. Macholl, et al., High-throughput high-volume nuclear imaging for preclinical in vivo compound screening(§), EJNMMI Res. 7 (2017) 33.

[69] A. Ganguly, S. Sharma, P. Papakonstantinou, J. Hamilton, Probing the thermal deoxygenation of graphene oxide using high-resolution in situ X-ray-based spectroscopies, J. Phys. Chem. C 115 (2011) 17009–17019.

[70] L.-N. Zhou, X.-T. Zhang, W.-J. Shen, S.-G. Sun, Y.-J. Li, Monolayer of close-packed Pt nanocrystals on a reduced graphene oxide (RGO) nanosheet and its enhanced catalytic performance towards methanol electrooxidation, RSC Adv. 5 (2015) 46017–46025.

[71] C. Botas, et al., Tailored graphene materials by chemical reduction of graphene oxides of different atomic structure, RSC Adv. 2 (2012) 9643–9650.